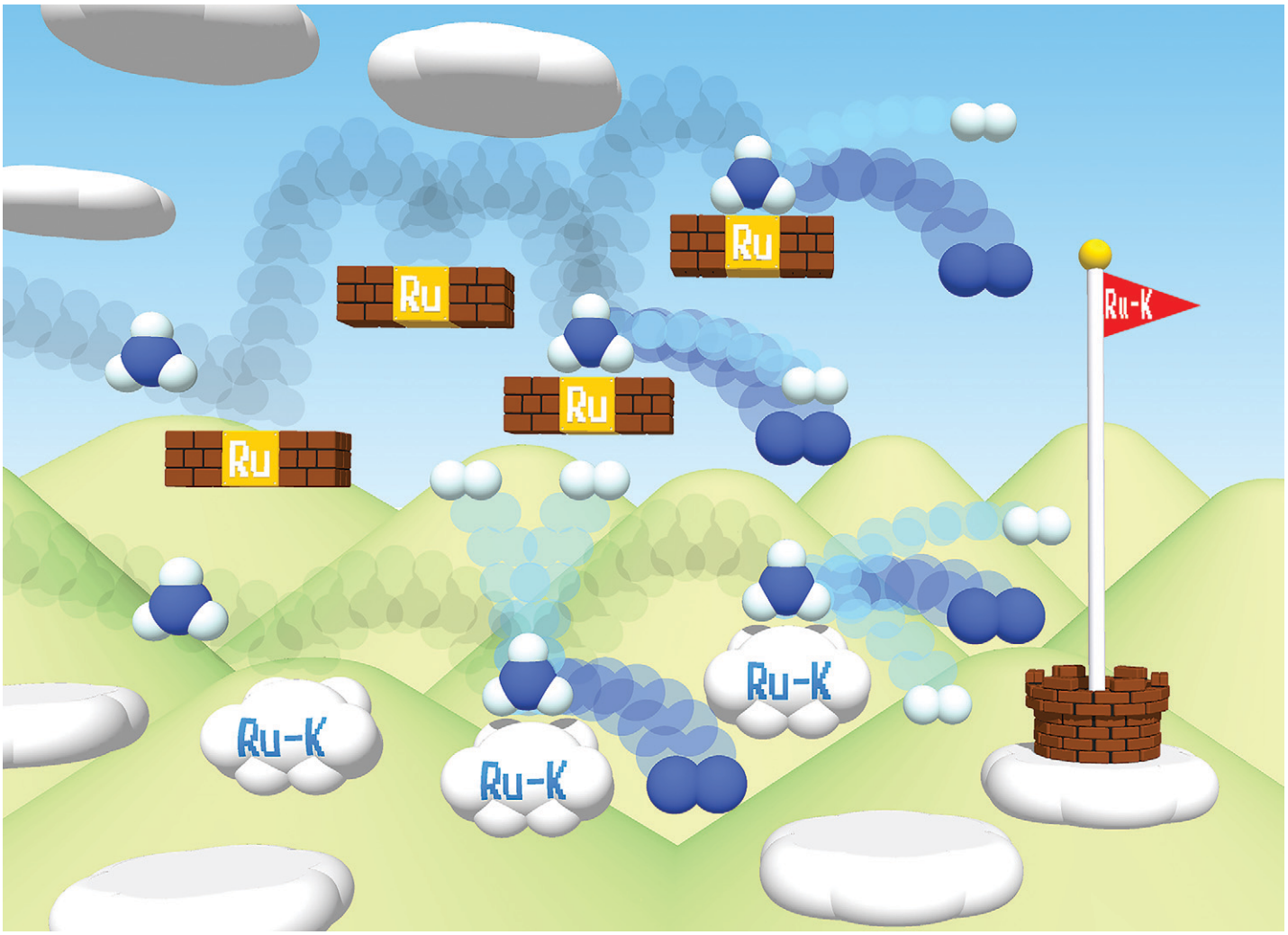

Showcasing research from Professor Castano's laboratory, Multiscale Reaction Engineering, King Abdullah University of Science and Technology (KAUST), Saudi Arabia.

Elucidating the rate-determining step of ammonia decomposition on Ru-based catalysts using *ab initio*-grounded microkinetic modeling

Game on! Try to win the trophy of clean hydrogen from ammonia by choosing the most favorable kinetic route and rate-determining step.

As featured in:

See Pedro Castaño *et al.*, *Catal. Sci. Technol.*, 2023, **13**, 2026.

ROYAL SOCIETY OF CHEMISTRY

rsc.li/catalysis

Registered charity number: 207890

Catalysis Science & Technology

ROYAL SOCIETY OF CHEMISTRY

PAPER

View Article Online
View Journal | View Issue

Cite this: *Catal. Sci. Technol.*, 2023, 13, 2026

Elucidating the rate-determining step of ammonia decomposition on Ru-based catalysts using *ab initio*-grounded microkinetic modeling†

Shekhar R. Kulkarni,‡[a] Natalia Realpe, ‡[a] Attada Yerrayya,[a] Vijay Kumar Velisoju, [a] Salvador Sayas, [a] Natalia Morlanes, [a] Jose Cerillo, [a] Sai P. Katikaneni,[b] Stephen N. Paglieri,[b] Bandar Solami,[b] Jorge Gascon [a] and Pedro Castaño *[a]

Decarbonizing the current energy system requires a shift toward renewable energy sources, among which ammonia is a remarkable hydrogen carrier. However, developing an efficient process for the catalytic decomposition of ammonia is still required. Here, we propose a combined modeling–experimental approach to elucidate the rate-determining step in ammonia decomposition on Ru-based catalysts. We characterize and test two supported Ru and Ru–K catalysts in the reaction. We develop several microkinetic models based on *ab initio* calculations considering different rate-determining steps and validate them with the results of packed bed experiments. For the method validation, we develop a fitting strategy based on modifying the lowest number of parameters from those initially obtained theoretically. A good agreement between the simulated and measured experimental ammonia conversions is obtained, thus widening our understanding of this critical hydrogen production process. The approach presented here allows distinguishing the rate-determining step accurately, and it could be applied to other catalytic systems used in ammonia decomposition to avoid over-relying on empirical models.

Received 12th January 2023,
Accepted 7th February 2023

DOI: 10.1039/d3cy00055a

rsc.li/catalysis

1. Introduction

The catalytic decomposition of ammonia (NH_3) has become a promising alternative over conventional reforming methods for on-site, high-pressure, high-purity hydrogen (H_2) generation. As an energy carrier, NH_3 is gathering increasing attention because of its high volumetric energy density, higher than that of some hydrocarbons such as methanol,[1] and well-established transportation and distribution networks.[2] Nevertheless, its most attractive feature is that high-purity, carbon-free H_2 can be obtained *via* NH_3 decomposition under relatively milder operating conditions of 400–600 °C and atmospheric pressure through a reverse Haber–Bosch process.[3,4] Moreover, this endothermic reaction ($-\Delta H_r$ = 46 kJ mol^{-1}) produces H_2 free from impurities that can be detrimental to potential applications involving fuel cells, where even traces of CO and CO_2 are poisonous.[5]

The NH_3 decomposition reaction is limited by the thermodynamic equilibrium, especially at high temperatures, which are necessary to overcome the reaction endothermicity. To circumvent these limitations, reactors fitted with H_2-selective membranes have been designed and experimentally tested. The selective and continuous removal of the generated H_2, delivered between 1 and 15 bar,[2,6,7] shifts the equilibrium toward the products. Moreover, the separation of pure H_2 from the generated nitrogen (N_2) or unreacted NH_3 is required because both impurities are detrimental to H_2 use and further applications. Despite the benefits of membrane reactors for this process, most new fundamental studies rely on conventional packed bed reactors to evaluate novel catalyst formulations.[8–10] To this aim, deepening the fundamental understanding of NH_3 decomposition *via* modeling is essential.

Single-metal catalysts have been predominantly used to study NH_3 decomposition because they can be easily simulated by density functional theory (DFT) calculations owing to their simplicity.[11,12] These calculations provide valuable insights into the kinetic mechanism of NH_3 decomposition[13–15] and the binding energies for N_2 desorption, as well as laying the basis for the rational design of catalysts.[16,17] Some DFT studies have also investigated multimetal-based catalysts, which can theoretically perform similarly to the benchmark Ru catalysts while being

[a] *KAUST Catalysis Center (KCC), King Abdullah University of Science and Technology (KAUST), Thuwal 23955-6900, Saudi Arabia.*
E-mail: pedro.castano@kaust.edu.sa
[b] *Carbon Management R&D Division, Research and Development Center, Saudi Aramco, Dhahran, 31311 Saudi Arabia*

† Electronic supplementary information (ESI) available. See DOI: https://doi.org/10.1039/d3cy00055a

‡ These authors contributed equally.

cheaper.[18] Thus, DFT is a valuable asset in understanding, designing and evaluating new catalysts for green H_2 production *via* catalytic NH_3 decomposition.

Ruthenium, the most active metal for NH_3 decomposition,[19] shows the highest reaction rate in the volcano plot of NH_3 decomposition activity *vs.* N_2 binding enthalpy among the studied active phases.[13,18] Thus, Ru-based catalysts can reach equilibrium conversion at temperatures below 500 °C and ambient pressure.[8] It is also known that alkaline promoters such as Cs, Na, La, and K are essential to improve the performance of Ru-based catalysts further.[20] In particular, K as a promoter improves Ru dispersion, thereby inhibiting Ru agglomeration under activation and reaction conditions. In addition, K acts as an electron donor[21] and increases the number of adsorption sites for H_2.[22] Considering that highly conductive supports like carbon nanotubes[21] are highly effective for NH_3 decomposition, an electron-donating promoter can be expected to enhance the catalytic activity. In fact, by combining Ru with K, the competitive adsorption of H_2 is reduced and the hydrogenation capability is decreased. Thus, it would be interesting to gain more insight into the promoting effect of K in this type of catalyst using *ab initio* calculations.

NH_3 decomposition proceeds on the catalyst surface through adsorption, sequential H abstractions, and desorption of N_2 and H_2. In this process, three reactions can be envisaged as plausible rate-determining steps (RDSs): NH_3 dissociation, NH dissociation, and N_2 desorption.[23] Although it is generally believed that N_2 desorption is the RDS for Ru-based catalysts, other steps have also been proposed (see selected examples in Fig. 1).

Owing to its simplicity, the Temkin–Pyzhev model (or modifications thereof) is extensively used to express the decomposition kinetics mathematically. The resulting rate expression contains a positive NH_3 concentration/partial pressure order (a) and a negative H_2 concentration/partial pressure order (b).[24,25] However, the model is derived by inherently assuming that the associative N_2 desorption is the RDS. Therefore, the reverse reaction of N_2 decomposition is ignored, and a power-law rate expression is built for which the relation $a = -0.67b$ holds. Although this model works for most active phases, experimental and, particularly, modeling studies have demonstrated deviations, as partly summarized in Fig. 1, in which N_2 desorption is not the RDS. Thus, the approach of using the Temkin–Pyzhev model and implicitly assuming an RDS needs to be revisited from the viewpoint of the reaction microkinetics. In this context, the experimental–modeling work of Ganley *et al.*[26] represents a landmark because it revealed that Ru (along with Ni) occupies a position near the intersection of two possible RDSs in a turnover frequency *vs.* N–H bond scission plot. Therefore, predicting the RDS for Ru-based catalysts is a challenging task. Sayas *et al.*[8] recently confirmed this hypothesis and showed that it was difficult to elucidate the RDS for an Ru–K/CaO catalyst. The proposed mechanistic models for the two possible RDSs, *i.e.*, N_2 desorption and N–H scission, afforded identical predictions against their lab-scale experimental data. Moreover, a power-law rate model (non-Temkin–Pyzhev, *i.e.*, $a \neq -0.67b$) offered the most straightforward and robust kinetic expression for the decomposition reaction among the detailed kinetic models. Despite the efforts devoted to unveiling the RDS for Ru-based catalysts *via* DFT and kinetic modeling studies, no conclusive answer has been reached yet. Similar results were obtained for Fe-based catalysts in a systematic experimental–modeling study.[27] In this regard, we recently showed through extensive experimental data fitting for various catalysts that a non-Temkin–Pyzhev kinetic expression containing the equilibrium constant can represent the reaction kinetics for the high-pressure production of H_2.[28]

To unravel the disparity related to the RDS, each catalytic system needs a closer look using multiple approaches above and beyond the classical Temkin–Pyzhev model.[29] The problem of misidentifying the RDS also goes hand in hand with regarding N as the most abundant reaction intermediate, which contrasts with the observations of several modeling studies.[23,30,31] Additionally, the temperature

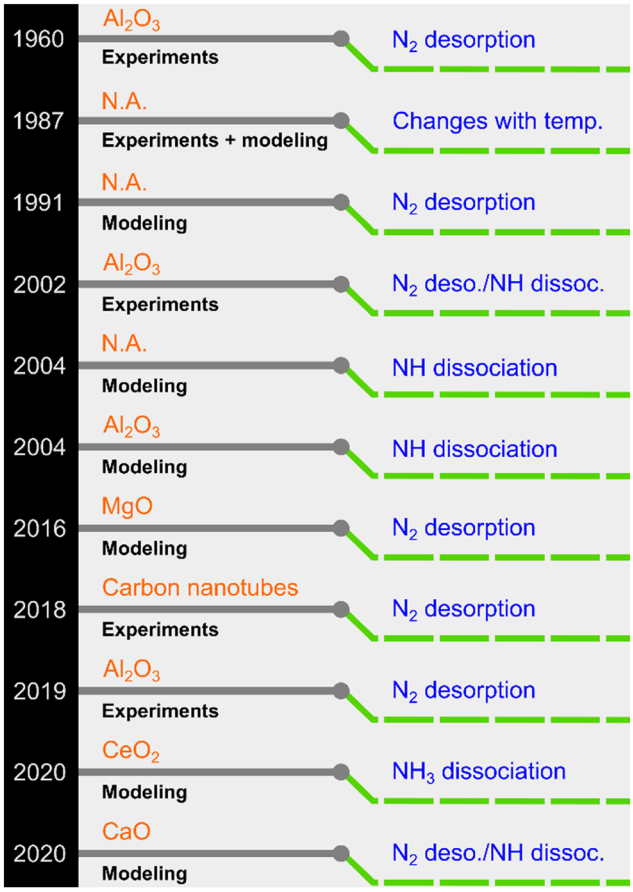

Fig. 1 A chronology of previously proposed rate-determining steps for Ru-based NH_3 decomposition catalysts (N.A.: ESI† not explicitly provided in the original work).

and NH_3 feed concentration greatly impact the surface species, thereby determining the most abundant reaction intermediate and, in turn, the RDS. A subsequent deviation from the Temkin–Pyzhev model is once again needed.[32]

Herein, we present an *ab initio*-grounded microkinetic modeling strategy for determining the RDS in the NH_3 decomposition reaction on Ru/CaO and Ru–K/CaO catalysts. In this combined experimental and modeling approach, we edit the parameters of first-principle calculations to reproduce the experimental results and discuss a plausible RDS for NH_3 decomposition. Three commonly considered RDSs are evaluated using differential and integral reactor models depending on the catalyst used. Using the derived microkinetic rate expression, without assuming relevant–irrelevant adsorbed species, the RDS can be predicted. We also examine the role of K as a promoter by systematically analyzing the species coverages for the two catalysts, leading to dissimilar experimental performances. The presented approach, a deviation from the classical Temkin–Pyzhev methodology, relies on combinations of *ab initio* calculations, lab-scale experiments, and appropriate reactor modeling to express the NH_3 decomposition kinetics.

2. Methods

2.1 Catalyst synthesis and characterization

As the Ru precursor, rehydrated $RuCl_3$ (Aldrich) was selected and incorporated onto a CaO support *via* incipient wetness impregnation using acetone for the Ru/CaO catalyst. For the Ru–K/CaO catalyst, after drying the Ru/CaO powder at 60 °C for 3 h, followed by thermal treatment under Ar at 500 °C for 3 h, a K promoter was introduced *via* incipient wetness impregnation using KOH in ethanol. Finally, a second thermal treatment was performed under Ar at 500 °C for 3 h to produce the desired Ru–K/CaO catalyst. The optimized catalyst compositions were 3%Ru/CaO and 3%Ru–10%K/CaO, respectively. More details about the catalyst synthesis protocols can be found in the ESI† in Fig. S1.

Transmission electron microscopy (TEM) of the samples was performed with a Titan Themis-Z microscope (Thermo-Fisher Scientific) operated at an accelerating voltage of 300 kV and a beam current of 0.5 mA.

NH_3 temperature-programmed desorption (NH_3-TPD) measurements were conducted using an Altamira AMI-200ip equipment. The catalyst (0.1 g) was reduced in H_2 at 500 °C for 1 h, cooled to 150 °C under H_2, and purged with an Ar flow for 0.5 h. After adsorbing NH_3 for 1 h at 100 °C, the sample was flushed in Ar for 0.5 h to remove the physisorbed NH_3. Finally, the temperature was increased linearly from 50 °C to 500 °C at a heating rate of 10 °C min^{-1} using Ar as a carrier gas, and the effluent was analyzed using a mass spectrometer. The results were analyzed according to a previously developed methodology, using eqn (1) to calculate the desorption energy (E_{des}):[33]

$$E_{des} = RT_{max}\left[\ln\left(\frac{vT_{max}}{\beta}\right) - 3.46\right] \quad (1)$$

where T_{max} is the maximum desorption temperature (K), v is the pre-exponential factor ($v = 10^{13}$ s^{-1} assuming first-order kinetics[23,34,35]), and β is the heating rate (K min^{-1}).

2.2 NH_3 decomposition experiments

Owing to the dampening effect of high pressure on NH_3 conversion, only the experimental data at atmospheric pressure was considered in this work for the modeling and fitting. The reaction temperature (200–500 °C), space velocity (9000–30 000 mL g_{cat}^{-1} h^{-1}), and partial pressures of feed NH_3 and H_2 (0–1 atm) were varied to obtain information about NH_3 conversion in a lab-scale packed bed reactor. An alumina coated-stainless steel reactor (PID Microactivity Reference system) with an internal diameter of 9 mm and a length of 170 mm was filled with 0.1 g catalyst sieved between 300 and 500 μm and 1 g SiC mixture to ensure a uniform heat distribution and avoid cold spots during the reaction. Ar was used as an internal standard, and the product stream was analyzed using a micro-gas chromatograph (micro-GC, 3000A, Agilent). Before the experiments, the catalyst was activated *in situ* with H_2 at 500 °C for 3 h. The effect of H_2 and NH_3 feed partial pressures was only examined on the Ru–K/CaO catalyst because of its higher activity. In total, 15 and 72 unique experimental data points were obtained for the Ru/CaO and Ru–K/CaO catalysts, respectively. Additional experimental details can be found in the works of Sayas *et al.*,[8] while the specific operating conditions are further listed in the captions.

2.3 Computational methods

Vienna *ab initio* simulation package was used to perform first-principles DFT calculations, and material studio and VESTA were used as the visualization software. The electron exchange and correlation interactions were modeled using the generalized gradient approximation[36] with the Perdew–Burke–Ernzerhof functional.[37] The electron–ion interactions were defined using the projector-augmented wave method. The vdW D3 correction proposed by Grimme was used to consider weak binding systems.[38] A plane-wave basis set was used to describe the valence electrons with an energy cut-off of 400 eV. The Brillouin zone, sampled at the Monkhorst–Pack 3 × 3 × 1 *k*-point grid,[39] was used to sample the Ru(111) surface and the Ru_2K_4 cluster on CaO(111). The choice of Ru-surface for the Ru/CaO catalyst and Ru–K cluster for the Ru–K/CaO catalyst stems from the respective active phases, as identified through multiple characterization techniques used in the original work.[8] The Ru(111) surface was modeled as a four-layer slab using a 3 × 3 supercell with 15 Å of vacuum between the slabs. The bottom two layers

were fixed, and the top two layers and adsorbates were relaxed. The CaO(111) surface was modeled as two layers, the bottom layer was fixed, and the top layer was relaxed. The equilibrium geometries were reached for all total energy optimizations once the atomic forces on every atom were smaller than 0.05 eV $Å^{-1}$ with a total energy convergence criterion of 1.0×10^{-6} eV. For the gas phase molecule, a cubic box of $15 \times 15 \times 15$ $Å^3$ was used. The transition states of the NH_3 decomposition elementary reaction steps were identified using the climbing nudged energy band method. The catalyst characterization results[40] indicated that Ru possessed a (111) surface plane. With the addition of K promoter to Ru, an Ru_2K_4 cluster was formed. As expected, CaO had a negligible effect on the Ru catalysts having pure surfaces compared with those with K-promoted surfaces. Therefore, the CaO(111) surface was used for the Ru–K catalyst.

To explain the surface chemistry of NH_3 decomposition on the Ru(111) surface and the Ru–K cluster, the adsorption energy (E_{ads}) and the reaction pathway were analyzed using DFT calculations. The following equation was used to calculate the E_{ads} of the species involved in the NH_3 decomposition mechanism, *i.e.*, reactants, intermediates, and products:[41,42]

$$E_{ads} = E_{adsorbate+Ru(111)} - E_{adsorbate} - E_{Ru(111)} \quad (2)$$

where $E_{adsorbate+Ru(111)}$ is the total energy of the adsorbed adsorbate on the Ru(111) surface and $E_{adsorbate}$ and $E_{Ru(111)}$ are the energy of the adsorbate in the gas phase and the bare Ru(111) surface. The individual optimized structures of catalyst surfaces, reactants, intermediates, and products are given in Fig. S3.† The E_{ads} values of all species are shown in Table S1,† with more negative values indicating a stronger adsorption.

The coadsorption energies of adsorbates were calculated using eqn (3):[43]

$$E_{coads} = E_{(a1+a2)/Ru(111)} - E_{a1} - E_{a2} - E_{Ru(111)} \quad (3)$$

where $E_{(a1+a2)/Ru(111)}$ is the total energy of the adsorbed adsorbates on the Ru(111) surface and E_{a1}, E_{a2}, and $E_{Ru(111)}$ are the energy of adsorbate1, adsorbate2 in the gas phase, and the bare Ru(111) surface.

To understand the mechanism of NH_3 decomposition, the transition states of various elementary steps were studied, which afforded the activation energies (E_{DFT}) and reaction energies (E_r) according to the following equations:

$$E_{DFT} = E_{TS} - E_{IS} \quad (4)$$

$$E_r = E_{FS} - E_{IS} \quad (5)$$

where E_{IS}, E_{TS}, and E_{FS} are the energies of the initial state, transition state, and final state, respectively.

Table 1 Elementary reactions modeled for catalytic NH_3 decomposition. R_i and R_{ii} are the forward and backward reactions, respectively

Reaction	Expression	Nomenclature
NH_3 adsorption	$NH_3 + * \leftrightarrow NH_3^*$	R_1, R_{11}
NH_3 dissociation	$NH_3^* + * \leftrightarrow NH_2^* + H^*$	R_2, R_{22}
NH_2 dissociation	$NH_2^* + * \leftrightarrow NH^* + H^*$	R_3, R_{33}
NH dissociation	$NH^* + * \leftrightarrow N^* + H^*$	R_4, R_{44}
N_2 desorption	$2N^* \leftrightarrow N_2 + 2^*$	R_5, R_{55}
H_2 desorption	$2H^* \leftrightarrow H_2 + 2^*$	R_6, R_{66}
Overall	$2NH_3 \rightarrow N_2 + 3H_2$	

2.4 Microkinetic modeling

For the microkinetic modeling, it was assumed that (i) all the species generated during the reactions are kinetically relevant, (ii) the surface is energetically uniform and the slow steps are partially reversible, and (iii) the surface sites are energetically uniform, *i.e.*, the adsorption of the species follows the Langmuir isotherm. Table 1 summarizes the series of reactions involved in the catalytic NH_3 decomposition, with the starting point being the adsorption of an NH_3 molecule on the catalyst surface.

The rate constants corresponding to these reactions can be expressed as follows:

$$k_i = k_{0,i} \exp\left(-\frac{E_i}{RT}\right) \quad (6)$$

$$k_{ii} = k_{0,ii} \exp\left(-\frac{E_{ii}}{RT}\right) \quad (7)$$

$$K_i = \frac{k_i}{k_{ii}} \quad (8)$$

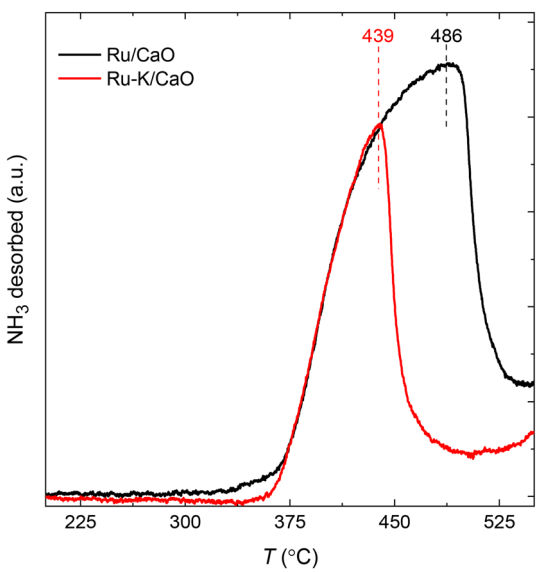

Fig. 2 NH_3 temperature-programmed desorption profiles of Ru/CaO and Ru–K/CaO catalysts after reduction at 500 °C.

where K_i is the equilibrium rate constant, which is defined as the ratio of the forward (k_i) to backward (k_{ii}) reaction rate constants. Here, the expressions for the NH_3 decomposition rate of the three plausible RDS previously identified in the literature are presented. Detailed derivations and procedures are provided in the ESI.† Pre-exponential factors were set in the order of 10^{13} s^{-1} in agreement with similar reported studies.[23,34,35]

Case A corresponds to NH_3 dissociation; case B represents N_2 desorption; while case C covers NH dissociation as the rate-determining step. The corresponding rate expressions, as obtained from the reaction microkinetics are presented further:

Case A:

$$r_2 = \frac{k_2 K_1 P_{NH_3}}{\left(1 + K_1 P_{NH_3} + \frac{P_{H_2}}{K_3 K_4 K_6}\sqrt{\frac{P_{N_2}}{K_5}} + \frac{1}{K_4}\sqrt{\frac{P_{N_2}}{K_5}\frac{P_{H_2}}{K_6}} + \sqrt{\frac{P_{N_2}}{K_5}} + \sqrt{\frac{P_{H_2}}{K_6}}\right)^2} \quad (9)$$

Case B:

$$r_5 = \frac{k_5 (K_1 K_2 K_3 K_4)^2 K_6{}^3 P_{NH_3}{}^2}{P_{H_2}{}^{3/2}\left(1 + K_1 P_{NH_3} + \frac{K_1 K_2 \sqrt{K_6}}{\sqrt{P_{H_2}}} P_{NH_3} + \frac{K_1 K_2 K_3 K_6}{P_{H_2}} P_{NH_3} + \frac{K_1 K_2 K_3 K_4 K_6{}^{3/2}}{P_{H_2}{}^{3/2}} P_{NH_3} + \sqrt{\frac{P_{H_2}}{K_6}}\right)^2} \quad (10)$$

Case C:

$$r_4 = \frac{k_4 K_1 K_2 K_3 K_6 (P_{NH_3})}{P_{H_2}\left(1 + K_1 P_{NH_3} + \frac{K_1 K_2 \sqrt{K_6}}{\sqrt{P_{H_2}}} P_{NH_3} + \frac{K_1 K_2 K_3 K_6}{P_{H_2}} P_{NH_3} + \sqrt{\frac{P_{N_2}}{K_5}} + \sqrt{\frac{P_{H_2}}{K_6}}\right)^2} \quad (11)$$

2.5 Fitting for a packed bed reactor

A one-dimensional model for a packed bed reactor was derived on the basis of the following simplifying assumptions: (i) steady-state operation, (ii) flow only along the axial direction of the reactor with no radial dispersion, (iii) isothermal operation, and (iv) negligible pressure drop along the axial direction of the reactor. For a packed bed reactor, the molar flow rate for each component in the reaction can be expressed as follows:

$$\frac{dF_i}{dz} = \nu(r_{rxn})\frac{A \times W_{cat}}{V} \quad (12)$$

where F_i represents the flow rate of the ith component, z represents the axial direction along the reactor, ν is a stoichiometric coefficient, A and V represent the area and volume of the catalytic bed, respectively, and W_{cat} is the catalyst weight. For the reaction rate (r_{rxn}), the expression described by eqn (9)–(11) was used. The activation energies for both the forward and backward elementary reactions (twelve in total) were fitted for the Ru/CaO and Ru–K/CaO catalysts. The variance of the error was computed according to eqn (14) and (15).

Parametric estimation was performed using the *fminsearch* function of Matlab, which finds the minimum of an unconstrained multivariable function using the derivative-free method, setting the sum of the squared residuals between the experimental data and the calculated data as the objective function. The NH_3 conversion described by eqn (13) was used as the fitting variable. The differential equations were solved using the *ode45* Matlab subroutine. The DFT-calculated values of the activation energies (E_{DFT}) were used as the seeding values to the optimization program and to recalculate these into E_{calc}.

$$X_{NH_3} = \frac{F_{NH_3,0} - F_{NH_3,L}}{F_{NH_3,0}} \times 100 \quad (13)$$

$$SSR = \min \sum_{i=1}^{i=n} \left(X_{NH_3}^{exp} - X_{NH_3}^{calc}\right)^2 \quad (14)$$

$$\sigma = \sqrt{\frac{SSR}{n-2}} \quad (15)$$

A similar approach involving fitting of the experimental data with microkinetic modeling and predicting the RDS was previously adopted for an Ni/Al_2O_3 catalyst by Armenise *et al.*,[23] although this work focused on a much smaller experimental dataset and DFT calculations were not performed. Instead, the authors introduced activation energy values found in the literature into microkinetic expressions for the respective RDSs. Additionally, the emphasis was placed on fitting ammonia, hydrogen, nitrogen adsorption/desorption energies rather than on the microkinetic steps leading from ammonia to hydrogen conversion.

3. Results and discussion

3.1 Catalyst characterization

The NH_3-TPD profiles (Fig. 2) of the supported Ru samples with and without K were recorded at a heating rate of 10 K min^{-1} after the reduction of the catalysts and subsequent NH_3 adsorption for 30 min at 100 °C. Both catalysts show similar desorption patterns, but the T_{max} of the sample with K is lower. The Ru–K/CaO catalyst exhibits a lower E_{des} (206.2 kJ mol^{-1}) than the Ru/CaO catalyst (E_{des} = 222.1 kJ mol^{-1}), indicating that the presence of K in the sample lowers the activation barrier for the NH_3 sorption process compared with the K-free Ru surface. As will be discussed later, these experimental results agree with the DFT theoretical calculations and suggest the superior catalytic activity of the K-based catalyst for NH_3 decomposition.

The morphology of both catalysts was analyzed using high-resolution transmission electron microscopy (HR-TEM) coupled with energy-dispersive X-ray spectroscopy (EDX) (Fig. S2†). The EDX analysis of both samples confirmed that the respective elements were present in the catalysts. TEM images of both the catalysts after reduction in H_2 flow at 500 °C for 3 h showed a fine distribution of Ru nanoparticles in the catalysts. However, in relative comparison, the doping of K in Ru/CaO resulted in a better dispersion with an average particle size of ~7 nm (with narrow distribution) compared to 9 nm for Ru/CaO. In addition, our previous[8] mapping results confirmed the presence of K throughout the catalyst surface, preferably located on top of the Ru nanoparticles.

3.2 DFT calculations

Four adsorption sites were examined for each adsorbate, *i.e.*, top, hcp, fcc, and bridge sites. The potential energy surface profile of H-abstraction from NH_y^* (y = 1–3) on Ru(111) and the Ru–K cluster is shown in Fig. 3. The structures of the initial, transition, and final states of all the elementary reactions on the Ru(111) surface and the Ru–K cluster are depicted in Fig. 4, and their most stable structures are shown in Fig. S3 and S4.† The decomposition of NH_3 proceeds through the following steps: NH_3 adsorption, H-abstraction from NH_y (y = 1–3), and associative desorption of N_2 and H_2. The E_{ads} values of NH_3 on Ru(111) and Ru–K(111) are −0.24 and −0.04 eV, respectively. The NH_3 molecule is preferentially adsorbed on the top site of the metal surface and the cluster. The N–H and Ru–H bond lengths on Ru(111) are 1.023 and 2.212 Å, respectively, and the H–N–H bond angles are 108.1° and 108.6° on Ru(111) and the Ru–K cluster, respectively. The bond lengths and angles are close to those of NH_3 in the gas phase (1.029 Å and 107.3°, respectively), indicating that the geometrical parameters remain virtually unaltered during the NH_3 adsorption on the metal surface.[44,45] The NH_2^* species is favorably adsorbed on both the bridge and the fcc site

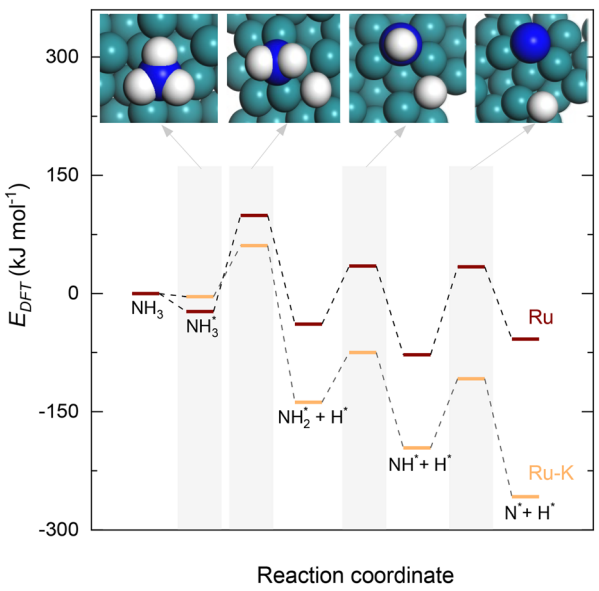

Fig. 3 Potential energy surface profile of the dehydrogenation of NH_y (y = 1–3) on Ru(111) and the corresponding transition states and Ru–K/CaO(111). The respective transition states of which are depicted in Fig. 4.

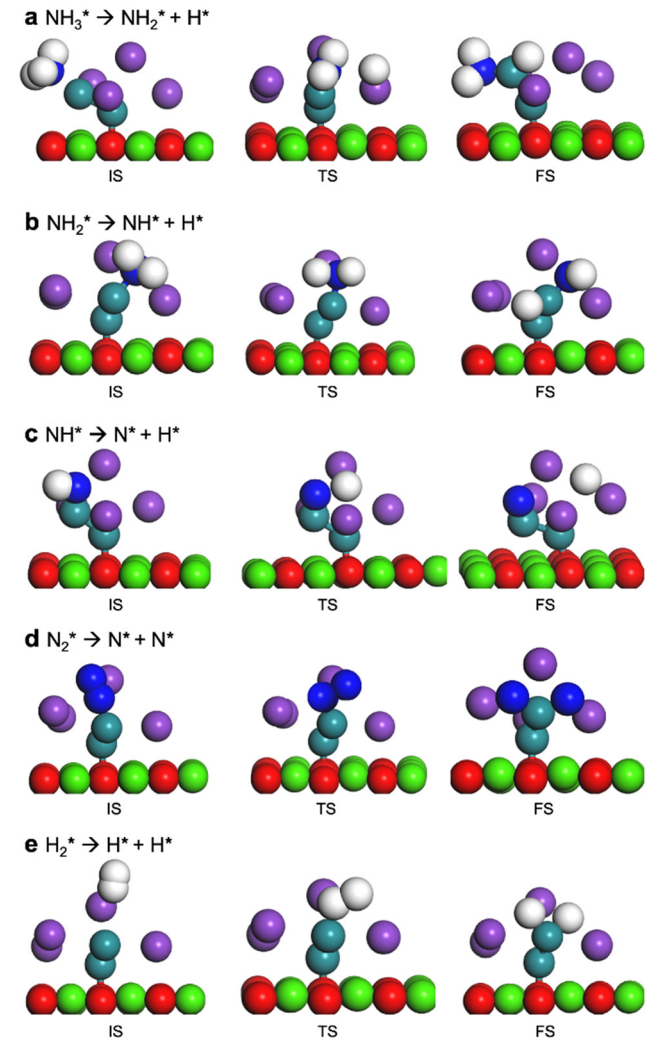

Fig. 4 Optimized structures of the initial, transition, and final states on the Ru–K/CaO(111) surface.

(hollow site) of the surface. The E_{ads} is slightly higher for the Ru–K cluster (−3.59 eV) than for the Ru(111) surface (−3.08 eV). The most stable adsorption site is fcc in the case of the adsorption of NH. The E_{ads} of NH is −4.97 on the Ru(111) surface and −5.29 eV on the Ru–K cluster, and the N–H and Ru–K bond lengths are 1.022 and 1.985 Å, respectively. Meanwhile, the adsorption of N* on the Ru–K cluster is almost 0.7 eV higher than on the Ru(111) surface, which means that the interaction of N* with K is stronger than that with Ru. It should be noted that the N* adatom acts as a descriptor for NH_y dehydrogenation reactions. The E_{ads} values of NH_y (y = 0–3) on both surfaces follow the order: N* > NH* > NH_2^* > NH_3^*; thus, the presence of fewer H atoms in NH_y renders the metal atoms more prone to adsorption.[11,43,46] Ru(111) and Ru–K clusters prefer fcc sites for H-adsorption, corresponding to E_{ads} of −2.87 and −3.1 eV, respectively. For H_2 and N_2, the most stable adsorption site is the top site. The H–H and N–N bonds are perpendicular to the surface and the cluster during the adsorption, which agrees with the literature.[47,48] The E_{ads} of N_2 is −0.7 eV for Ru(111) and −1.72 eV for the Ru–K cluster.

The most stable coadsorbed structures of NH_y^* (y = 0–3) and H* on Ru(111) surfaces, *i.e.*, NH_2^*/H* (bridge/fcc), NH*/H* (fcc/fcc), N*/H* (fcc/fcc), and N*/N* (fcc/fcc), are depicted in Fig. S1.† The E_{coads} of NH_2^* + H*, NH* + H*, N* + H*, and N* + N* on the Ru–K cluster are −6.95, −8.52, −9.81, and −12.63 eV, respectively. Table 2 shows that these values are higher than those for the Ru(111) surface. The sum of the individual energies is higher than the E_{coads} for the Ru(111) surface, indicating a repulsive interaction between individual adsorbates, which agrees with the literature.[44,45,48]

Upon the cleavage of the H* atom from NH_3^* to form NH_2^* and H* *via* dehydrogenation, the formed NH_2^* moves to the bridge site, and the H* atom is adsorbed on the fcc site. This process proceeds through a transition state with an energy barrier of 1.27 eV in the case of the Ru(111) surface and 0.68 eV for the Ru–K cluster, which is lower than that of some of the reported studies.[34,49,50] The N–H bond length increases from 1.023 to 1.46 Å at the transition state. The first dehydrogenation reaction is exothermic on the Ru(111) surface and the Ru–K cluster. The second step is the dehydrogenation of NH_2^* to generate NH* and H*, for which the energy barrier is 0.77 eV for Ru(111) and 0.66 eV for the Ru–K cluster, and the respective reaction energies are −0.41 and −0.6 eV, which means that the reaction is exothermic. The reported values of the energy barrier for this reaction are 0.73 eV on Cu(100),[51] 0.59 eV on Ni(111),[11] 1.63 eV on Ni(100), 1.59 eV on (Cu(111),[43] 1.54 on Pd(111),[43] 0.24 eV on Fe(110),[11] and 0.21 eV on Co(111).[11] NH* and H* are adsorbed on neighboring fcc sites. The formed NH* can further decompose to N* and H*, the H* adatom is adsorbed on the adjacent fcc site, and the N* atom remains on the same site. The energy barrier required to form N* and H* on the Ru(111) surface is 1.17 eV, and the reaction energy is 0.21 eV, which is endothermic.

In contrast, adding K to the catalyst reduces the energy barrier from 1.17 to 0.92 eV, and the reaction energy shows an exothermic value of −0.65 eV (Fig. 1). The recombination of the formed N atoms from the decomposition of NH to form N_2 shows an energy barrier of 1.82 eV in the case of the Ru(111) surface and 1.24 eV for the Ru–K cluster. This decrease in the energy barrier can be attributed to the surface structural and electronic effects derived from the presence of neighboring atoms Ru and K, as was previously reported by Sayas *et al.*[8] The associative desorption of H atoms to form H_2 proceeds with an energy barrier of 1.22 eV on Ru(111) and 1.88 eV on the Ru–K cluster. The forward reaction is

Table 2 Adsorption energies (eV) for different species present in the NH_3 decomposition process on pure Ru(111) and Ru–K/CaO surfaces

Species	Site	Ru(111)[a]	Ru(111)[b]	Ru–K[b]
NH_3^*	Top	−0.88	−0.24	−0.04
NH_2^*	Bridge	−3.05	−3.08	−3.59
NH*	fcc	−4.94	−4.97	−5.29
N*	fcc	−5.54	−5.83	−6.51
H*	fcc	−2.89	−2.87	−3.1
N_2	Top	−0.66	−0.70	−1.72
NH_2^* + H*	Bridge + fcc	−6.79	−5.95	−6.95
NH* + H*	fcc + fcc	−7.26	−7.82	−8.52
N* + H*	fcc + fcc	−7.88	−8.64	−9.81
N* + N*	fcc + fcc	−11.94	−11.52	−12.63

[a] US potential. [b] PBE.

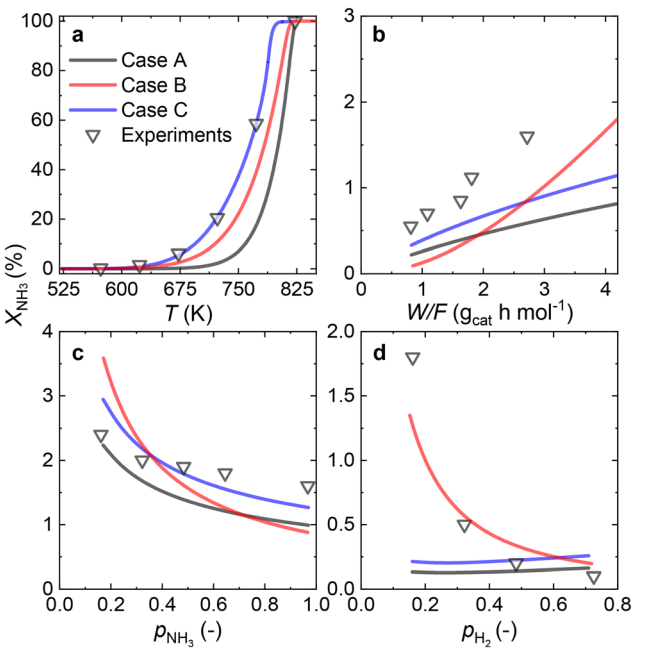

Fig. 5 Comparison of fitting predictions *via* differential reactor modeling for all the possible rate-determining steps (solid lines) *vs.* experimental measurements (triangles) for the Ru/CaO catalyst under various operating conditions: (a) NH_3 conversion (X_{NH_3}) *vs.* temperature, (b) X_{NH_3} *vs.* space velocity (W/F), (c) X_{NH_3} *vs.* NH_3 partial pressure (p_{NH_3}), and (d) X_{NH_3} *vs.* H_2 partial pressure (p_{H_2}). W_{cat} = 0.2 g; $F_{NH_3;0}$ = 30 NmL min^{-1}; P = 1 bar.

exothermic with reaction energies values of −1.22 and −1.73 eV on Ru(111) and Ru–K, respectively.

Overall, the stepwise dehydrogenation of NH_3 preferentially occurs on the Ru–K cluster, which is thermodynamically and kinetically favorable. The E_{ads} values are consistent with the literature regardless of the metal surface.[11,34,43–45,49,50] For instance, the energy barrier for the associative desorption of N on the Ru(111) surface and the Ru–K cluster is much lower than the values of 2.51 eV on Ru(001),[31] 2.56 eV on Mo_2N(100),[52] 3.22 eV on MoN(100),[52] 2.85 eV on Fe(100),[11] 1.86 eV on Ni(111),[11] and 1.86 eV on Co(111)[11] surfaces. The obtained results suggest that the associative desorption of N on the Ru(111) surface and the Ru–K cluster occurs easily compared with that on other metals. In the case of the Ru(111) surface, the RDS is the associative desorption of N*.

3.3 Ru/CaO catalyst

Since most of the experimental data gathered for the Ru/CaO catalyst falls within the low values of NH_3 conversion, two approaches can be considered for RDS prediction: differential reactor modeling and integral reactor modeling.

3.3.1 Differential reactor modeling. As depicted in Fig. 5(a), the DFT-predicted activation energies for Case A (NH_3 dissociation) approximately match the experimental trends for the temperature dependence of conversion. However, the predictions are poor for the space velocity variations. Consequently, for the operating conditions and the catalyst configurations tested, NH_3 dissociation could not be the RDS. Similarly, N_2 desorption (Case B) can be ruled out as the RDS; although the predictions are closer to the experimental data, they are not ideal. Meanwhile, the predictions for NH dissociation being the RDS (Case C: NH dissociation), as shown in Fig. 5(c), yield a perfect match. Further, the rate of NH_3 decomposition, as predicted by eqn (11) for this RDS, explicitly contains most of the activation energies, unlike in Case A or B. This observation, combined with the DFT-predicted energy barrier for reaction R_4, indicates that the NH scission, rather than the NH_3 scission, is likely the RDS.

3.3.2 Integral reactor modeling. Fig. 6 compares the fitting for the three possible RDSs against the experimental dataset for the NH_3 conversion as a function of temperature, space velocity, and NH_3 and H_2 partial pressures. All the cases can accurately predict the S-shaped conversion profiles as a function of temperature. For the rest of the parameters, Case A matches the experimental trends (especially NH_3 conversion *vs.* temperature and NH_3 partial pressures) but not the exact values, failing especially for the variation in space velocity and feed H_2 partial pressure (R^2 = 0.91). A similar result was found for Case B, for which the comparisons are significantly improved, with a good match for the conversion–temperature plot (R^2 = 0.97). Meanwhile,

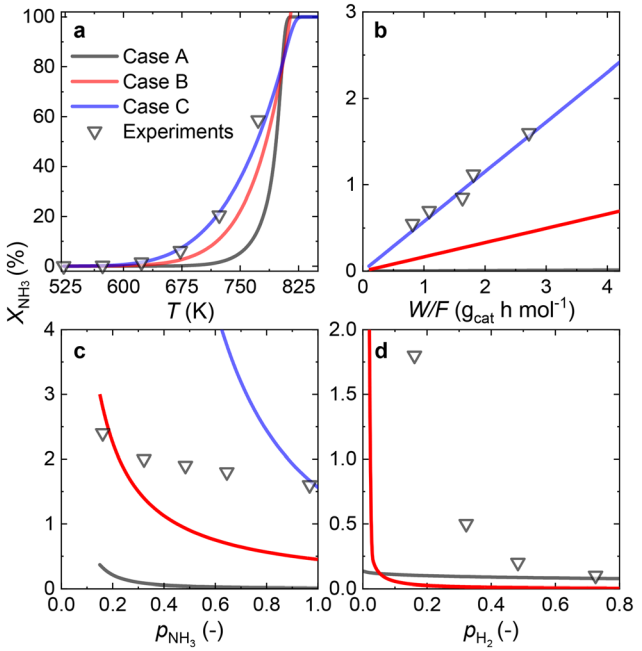

Fig. 6 Comparison of fitting predictions *via* integral reactor modeling for all the possible rate-determining steps (solid lines) *vs.* experimental measurements (triangles) for the Ru/CaO catalyst under various operating conditions: (a) NH_3 conversion (X_{NH_3}) *vs.* temperature, (b) X_{NH_3} *vs.* space velocity (W/F), (c) X_{NH_3} *vs.* NH_3 partial pressure (p_{NH_3}), and (d) X_{NH_3} *vs.* H_2 partial pressure (p_{H_2}). W_{cat} = 0.2 g; $F_{NH_3;0}$ = 30 NmL min^{-1}; P = 1 bar.

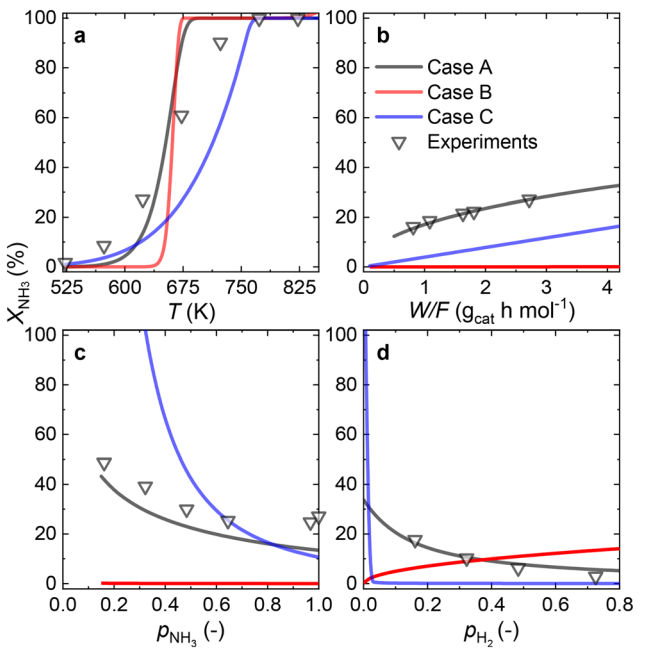

Fig. 7 Comparison of fitted model predictions for all the possible rate-determining steps (solid lines) *vs.* experimental measurements (triangles) for the Ru–K/CaO catalyst under various operating conditions: (a) NH_3 conversion (X_{NH_3}) *vs.* temperature, (b) X_{NH_3} *vs.* space velocity (W/F), (c) X_{NH_3} *vs.* NH_3 partial pressure (p_{NH_3}), and (d) X_{NH_3} *vs.* H_2 partial pressure (p_{H_2}). W_{cat} = 0.2 g; $F_{NH_3;0}$ = 30 NmL min^{-1}; P = 1 bar.

Case C shows the best fitting (R^2 = 0.99) in the temperature profile, space velocity, and NH_3 and H_2 partial pressures. By combining the presented fitting with the values of the activation energies (Table S2†), NH dissociation can be proposed as the RDS for the Ru/CaO catalyst.[26] A more detailed discussion of the fitted values of the activation energies and their implications is presented in Section 3.6.

Both approaches predict that NH dissociation (Case C) is the most probable RDS for NH_3 decomposition on the Ru/CaO catalyst for the experimental data obtained using a laboratory-scale packed bed reactor.

3.4 Ru–K/CaO catalyst

Owing to the high NH_3 conversions (>25%) observed for the Ru–K/CaO catalyst for most of the operating conditions, by definition, only the integral reactor model can be implemented. Fig. 7 compares the results of the experimental data fitting for the Ru–K/CaO catalyst using the integral approach. Similar to the K-free Ru catalyst, all the cases considered predict well the S-shaped behavior of the NH_3 conversion.

Case B could not be the RDS due to a poor overall fitting across the tested experimental variables (R^2 = 0.95). Case C matches most experimental data except for the variation in H_2 partial pressure (R^2 = 0.68). Case A shows the best match for all the variables, giving a near-perfect prediction for NH_3 conversion across a wide range of conditions (R^2 = 0.99). According to the good fitting results and the values of the optimized activation energies, NH_3 dissociation (Case A) can be proposed as the RDS over the Ru–K/CaO catalyst. Table S3† presents the variance of fitted activation energies compared with the DFT-predicted values. The integral approach presented here can successfully predict the RDS for Ru/CaO and Ru–K/CaO catalysts. However, owing to its higher activity than the K-free catalyst, the differential approach is not suitable for predicting the RDS for the Ru–K catalyst.

Fig. 8 summarizes the differences in activation energies between DFT-calculated values (E_{DFT}) and the corresponding recalculated using the fitting methodology (E_{calc}). Fig. 8(a) and (b) are values with the proposed rate-determining steps (Cases A–C) for Ru/CaO and Ru–K/CaO catalysts, respectively. Following trends are observed regarding DFT calculations: Case A, for both the catalysts, typically underpredicts the forward and over-predicts the backward reaction activation energies. While both Case B and Case C mostly overpredict both the forward and the backward reaction activation energies. The experimental non-idealities exist on the catalyst and reactor-scale non-homogeneities, while the DFT simulates ammonia decomposition in a model environment and allows idealistic

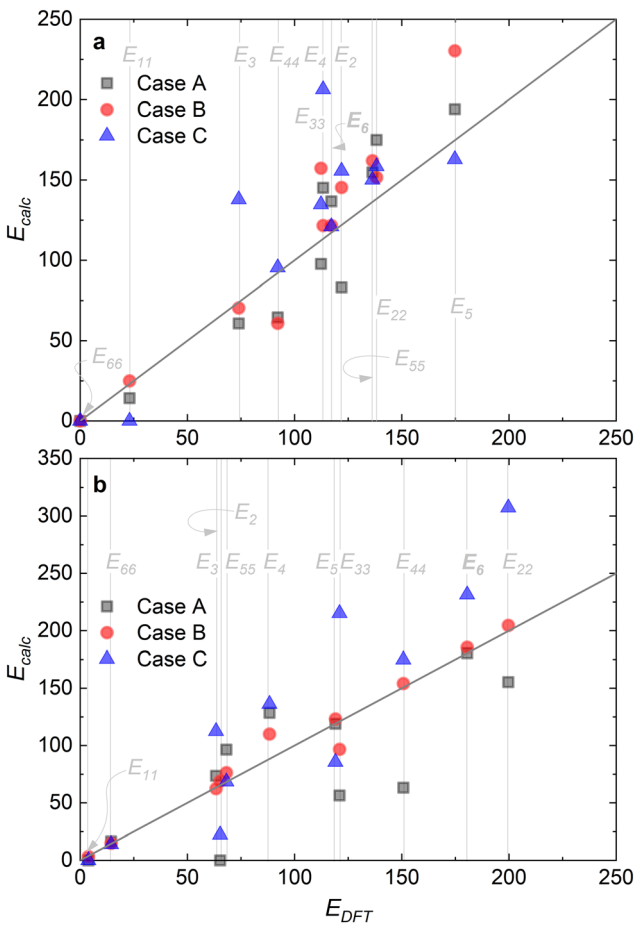

Fig. 8 Comparison *via* parity plots of the DFT-calculated activation energies (E_{DFT}) and those predicted *via* fitting (E_{calc}): (a) Ru/CaO; (b) Ru–K/CaO.

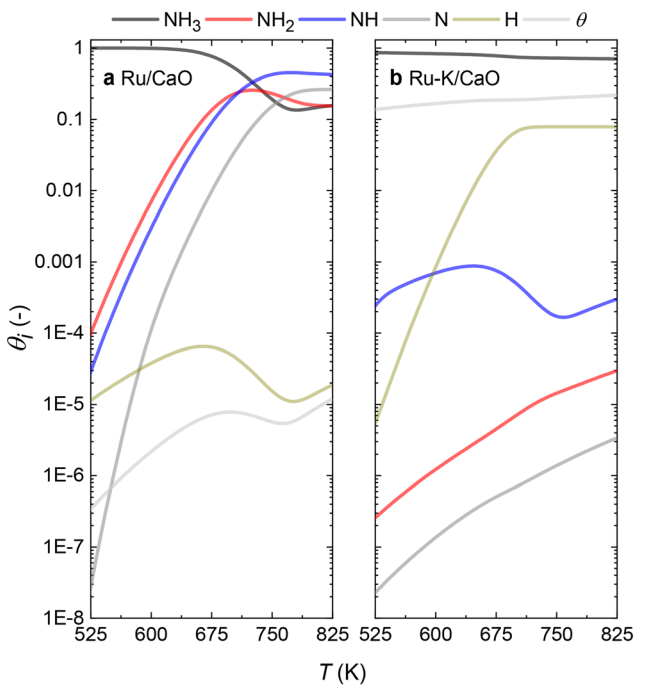

Fig. 9 Comparison of the species coverage at the steady state on (a) Ru/CaO; Case C (NH dissociation) and (b) Ru–K/CaO; Case A (NH_3 dissociation) as the rate-determining steps, respectively.

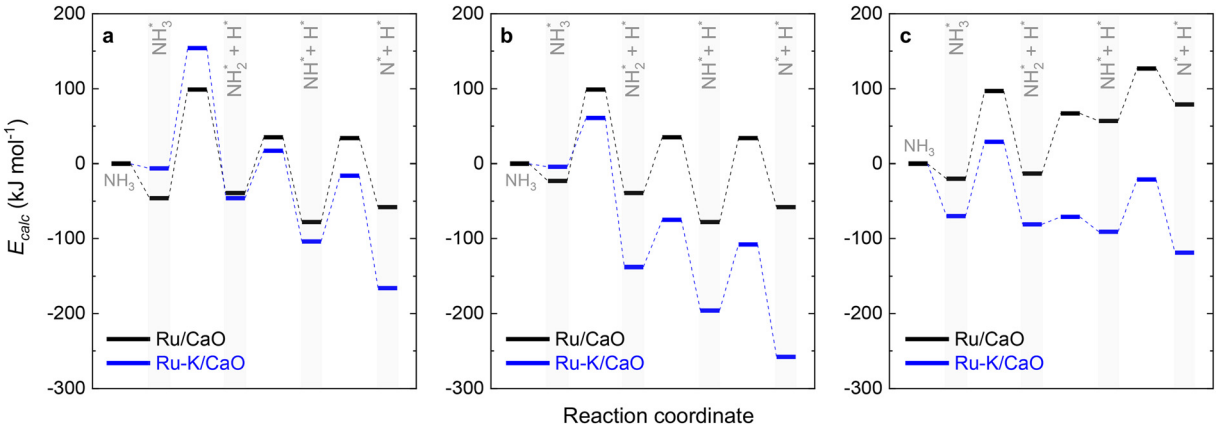

Fig. 10 Potential surface diagrams considering the obtained activation energies from the fitted models: (a) Case A (NH_3 dissociation); (b) Case B (N_2 desorption); and (c) Case C (NH dissociation).

molecule-active phase interactions. Despite these disparities in the two scales of operations, the modeling-fitted activation energies are relatively similar to the DFT calculated ones, underlining the validity and scalability of the approach that is based on coupling DFT and microkinetics. While focusing on the respective proposed RDSs, delta E values of the Ru/CaO catalyst are higher (~90 kJ mol^{-1}) against those of Ru–K/CaO (~35 kJ mol^{-1});[8] which could further be related to the reduced activation energies upon K-promotion as initially reported.

3.5 Coverages of species

With the activation energies obtained for the RDSs for both catalysts in hand, the fractional coverages of each species (θ_i) can be calculated. The results for both catalysts at steady-state conditions (case C for the Ru/CaO and case A for the Ru–K/CaO catalyst) are represented in Fig. 9. For each of the cases considered, while solving the differential equations of species balance, time is noted for which all the coverages reach a steady value. According to the DFT-calculated activation energies, the system takes ~0.1 s to achieve stable coverages and 0.2 and 0.3 s, respectively, for K-free (case C) and K-promoted Ru catalysts (case A).

The steady state is reached at different time scales for the Ru and Ru–K catalysts, consistent with the experimentally observed decrease in the E_{calc} for the latter. For the coverages corresponding to the NH dissociation as RDS for the Ru/CaO catalyst, the catalyst surface is fully occupied by NH_3^* species at lower temperatures, indicating a lack of catalytic activity. However, the NH_3^* species drastically disappear at higher temperatures from the surface and are mainly replaced with NH* species. Under these conditions, N* and NH_2^* species are also abundant; the former stems from the partial reaction and the latter from inhibiting the reaction due to the presence of abundant NH* species. From a microkinetic point of view, when NH dissociation is the RDS, the reaction progression toward the formation of N* and H* species and eventually toward the products is inhibited by the occupancy of the catalyst sites by NH* species. The simulated coverages presented in Fig. 9(a) represent well the case for the Ru/CaO catalyst under study in the present work. It is predicted that the H* coverage and free sites are negligible.

Adding K to the catalyst considerably changes the catalyst surface at low and high temperatures. Irrespective of the reaction temperature, the surface is majorly covered by NH_3^* species, with the rest remaining as free sites, demonstrating the effect of the promotion of the noble metal with K on the reaction mechanism. According to the sequential reaction mechanism at the microkinetic scale leading to product desorption, no NH_2^*, NH*, and N* species are present on the catalyst surface; there are only traces of H* species at a higher temperature, which is in accord with previous reports showing that the addition of K increases the number of H-adsorption sites.[22] Thus, the coverage analysis provides a unique insight into the role of K as a promoter, which enhances the NH_3 decomposition performance by altering the RDS at the microkinetic level.

Fig. 10 collectively compares the potential surfaces for the three RDSs studied for both catalysts. For all the cases, adding K to the catalyst leads to the formation of Ru–K clusters and favors the decomposition reaction thermodynamically. The DFT-predicted transition states depicted in Fig. 4 differ from those in Fig. 10 due to differences in the reaction potentials of the E_{calc} obtained using the present approach. However, the exact nature of each transition state is not significant compared with their progression.

4. Conclusions

An experimentally validated modeling approach comprising DFT calculations, microkinetic modeling, and fitting is presented to investigate the catalytic NH_3 conversion to pure H_2 over Ru/CaO and Ru–K/CaO catalysts.

Catalyst characterization showed a lowered activation barrier for the NH_3 sorption process on the Ru–K/CaO catalyst. Theoretical calculations revealed the most stable

catalyst–adatom structures formed during NH_3 decomposition for both catalysts. Fitting of the experimental data in the first step predicted NH dissociation as the RDS for the Ru/CaO catalyst, whereas NH_3 dissociation is the RDS for the Ru–K/CaO catalyst. The predicted RDSs for these catalysts differ from those proposed in the literature, partly due to an overreliance on the Temkin–Pyzhev model and a lack of combined DFT/microkinetic-based reaction analyses. Finally, comparing the species coverages predicted by the microkinetic model sheds light on the role of K promotion, revealing that the addition of K to the catalyst alters its surface and selectively, promoting the N_2 desorption and thereby altering the RDS.

Unlike the empirically derived Temkin–Pyzhev model, the approach presented in this work is purely based on *ab initio* theories and can thus offer a new platform for the design of improved catalysts for NH_3 decomposition.

Nomenclature

Abbreviations

RDS	Rate-determining step
DFT	Density functional theory
TPD	Temperature-programmed desorption
SSR	Residual sum of squares

Nomenclature

a	Ammonia reaction order (−)
b	Hydrogen reaction order (−)
E_{des}	Desorption energy (kJ mol^{-1})
R	Universal gas constant (8.314 kJ mol^{-1} K^{-1})
T	Temperature (K)
T_{max}	Maximum desorption temperature (K)
β	Heating rate (K min^{-1})
v	Pre-exponential factor (10^{13} s^{-1} assuming first-order kinetics)
$E_{(a1+a2)/Ru(111)}$	Total energy of adsorbed adsorbates on Ru(111) surface (kJ mol^{-1})
E_{a1}	Energy of adsorbate1 in the gas phase (kJ mol^{-1})
E_{a2}	Energy of adsorbate2 in the gas phase (kJ mol^{-1})
E_{ads}	Adsorption energy of species (kJ mol^{-1})
$E_{adsorbate+Ru(111)}$	Total adsorption energy on the Ru(111) surface (kJ mol^{-1})
$E_{adsorbate}$	Adsorption energy in the gas phase (kJ mol^{-1})
E_{calc}	Activation energy calculated by fitting (kJ mol^{-1})
E_{coads}	Coadsorption energy of adsorbates (kJ mol^{-1})
E_{DFT}	Activation energy calculated by DFT (kJ mol^{-1})
E_{FS}	Potential energy of the final state (kJ mol^{-1})
E_{IS}	Potential energy of the initial state (kJ mol^{-1})
E_{TS}	Potential energy of the transition state (kJ mol^{-1})
$E_{Ru(111)}$	Adsorption energy on the bare Ru(111) surface (kJ mol^{-1})
F	Flow rate (mL min^{-1})
$F_{NH_3,0}$	Ammonia feed flow rate (mL min^{-1})
k_i	Forward reaction rate (s^{-1})
k_{ii}	Backward reaction rate (s^{-1})
K_i	Equilibrium rate constant (−)
P	Pressure (atm)
V	Reactor volume (mL)
W_{cat}	Catalyst mass (g)
W/F	Space velocity (g h^{-1} mol$_{NH_3}$)
X_{NH_3}	Ammonia conversion (%)
Z	Axial direction (−)
θ_i	Fractional coverage of each species (−)

Conflicts of interest

There are no conflicts to declare.

Acknowledgements

The authors gratefully acknowledge the financial support provided by Saudi Aramco and the resources and facilities provided by the King Abdullah University of Science and Technology (KAUST). The authors acknowledge the KAUST Supercomputing Laboratory (KSL) for providing high-performance computational resources.

References

1 S. Mukherjee, S. V. Devaguptapu, A. Sviripa, C. R. F. Lund and G. Wu, *Appl. Catal., B*, 2018, **226**, 162–181.
2 N. Itoh, A. Oshima, E. Suga and T. Sato, *Catal. Today*, 2014, **236**, 70–76.
3 K. E. Lamb, M. D. Dolan and D. F. Kennedy, *Int. J. Hydrogen Energy*, 2019, **44**, 3580–3593.
4 F. Schüth, R. Palkovits, R. Schlögl and D. S. Su, *Energy Environ. Sci.*, 2012, **5**, 6278–6289.
5 R. Lan, J. T. S. Irvine and S. Tao, *Int. J. Hydrogen Energy*, 2012, **37**, 1482–1494.
6 Z. Zhang, S. Liguori, T. F. Fuerst, J. D. Way and C. A. Wolden, *ACS Sustainable Chem. Eng.*, 2019, **7**, 5975–5985.
7 J. L. Cerrillo, N. Morlanés, S. R. Kulkarni, N. Realpe, A. Ramírez, S. P. Katikaneni, S. N. Paglieri, K. Lee, A. Harale, B. Solami, A. Jamal, S. Mani Sarathy, P. Castaño and J. Gascon, *Chem. Eng. J.*, 2022, **431**, 134310.
8 S. Sayas, N. Morlanés, S. P. Katikaneni, A. Harale, B. Solami and J. Gascon, *Catal. Sci. Technol.*, 2020, **10**, 5027–5035.
9 N. Morlanés, S. Sayas, G. Shterk, S. P. Katikaneni, A. Harale, B. Solami and J. Gascon, *Catal. Sci. Technol.*, 2021, **11**, 3014–3024.
10 M. Pinzón, A. Romero, A. de Lucas Consuegra, A. R. de la Osa and P. Sánchez, *J. Ind. Eng. Chem.*, 2021, **94**, 326–335.
11 X. Duan, J. Ji, G. Qian, C. Fan, Y. Zhu, X. Zhou, D. Chen and W. Yuan, *J. Mol. Catal. A: Chem.*, 2012, **357**, 81–86.

12 S. Stolbov and T. S. Rahman, *J. Chem. Phys.*, 2005, **123**, 1–6.
13 A. Boisen, S. Dahl, J. K. Nørskov and C. H. Christensen, *J. Catal.*, 2005, **230**, 309–312.
14 L. Yu and F. Abild-Pedersen, *ACS Catal.*, 2017, **7**, 864–871.
15 M. D. Esrafili and R. Nurazar, *Struct. Chem.*, 2015, **26**, 799–807.
16 K. Ogasawara, T. Nakao, K. Kishida, T. N. Ye, Y. Lu, H. Abe, Y. Niwa, M. Sasase, M. Kitano and H. Hosono, *ACS Catal.*, 2021, **11**, 11005–11015.
17 C. Zhou, K. Wu, H. Huang, C. F. Cao, Y. Luo, C. Q. Chen, L. Lin, C. Au and L. Jiang, *ACS Catal.*, 2021, **11**, 10345–10350.
18 D. A. Hansgen, D. G. Vlachos and J. G. Chen, *Nat. Chem.*, 2010, **2**, 484–489.
19 H. Fang, D. Liu, Y. Luo, Y. Zhou, S. Liang, X. Wang, B. Lin and L. Jiang, *ACS Catal.*, 2022, **12**, 3938–3954.
20 C. Chen, K. Wu, H. Ren, C. Zhou, Y. Luo, L. Lin, C. Au and L. Jiang, *Energy Fuels*, 2021, **35**, 11693–11706.
21 A. K. Hill and L. Torrente-Murciano, *Int. J. Hydrogen Energy*, 2014, **39**, 7646–7654.
22 W. Pyrz, R. Vijay, J. Binz, J. Lauterbach and D. J. Buttrey, *Top. Catal.*, 2008, **50**, 180–191.
23 S. Armenise, E. García-Bordejé, J. L. Valverde, E. Romeo and A. Monzón, *Phys. Chem. Chem. Phys.*, 2013, **15**, 12104–12117.
24 K. Lamb, S. S. Hla and M. Dolan, *Int. J. Hydrogen Energy*, 2019, **44**, 3726–3736.
25 B. Wang, H. Kong, H. Wang, Y. Wang and X. Hu, *Int. J. Hydrogen Energy*, 2019, **44**, 26874–26887.
26 J. C. Ganley, F. S. Thomas, E. G. Seebauer and R. I. Masel, *Catal. Lett.*, 2004, **96**, 117–122.
27 S. A. Vilekar, I. Fishtik and R. Datta, *Chem. Eng. Sci.*, 2012, **71**, 333–344.
28 N. Realpe, S. R. Kulkarni, J. L. Cerrillo, N. Morlanés, G. Lezcano, S. P. Katikaneni, S. N. Paglieri, M. Rakib, B. Solami, J. Gascon and P. Castaño, *React. Chem. Eng.*, 2023, DOI: **10.1039/D2RE00408A**, Accepted.
29 T. E. Bell and L. Torrente-Murciano, *Top. Catal.*, 2016, **59**, 1438–1457.
30 S. R. Deshmukh, A. B. Mhadeshwar and D. G. Vlachos, *Ind. Eng. Chem. Res.*, 2004, **43**, 2986–2999.
31 A. B. Mhadeshwar, J. R. Kitchin, M. A. Barteau and D. G. Vlachos, *Catal. Lett.*, 2004, **96**, 13–22.
32 V. Prasad, A. M. Karim, A. Arya and D. G. Vlachos, *Ind. Eng. Chem. Res.*, 2009, **48**, 5255–5265.
33 B. Lin, K. Wei, X. Ma, J. Lin and J. Ni, *Catal. Sci. Technol.*, 2013, **3**, 1367–1374.
34 G. Novell-Leruth, A. Valcarcel, J. Pérez-Ramírez and J. M. Ricart, *J. Phys. Chem. C*, 2007, **111**(2), 860–868.
35 V. Prasad, A. M. Karim, A. Arya and D. G. Vlachos, *Ind. Eng. Chem. Res.*, 2009, **48**, 5255–5265.
36 J. P. Perdew, K. Burke and M. Ernzerhof, *Phys. Rev. Lett.*, 1996, **77**, 3865–3868.
37 J. P. Perdew, J. A. Chevary, S. H. Vosko, K. A. Jackson, M. R. Pederson, D. J. Singh and C. Fiolhais, *Phys. Rev. B: Condens. Matter Mater. Phys.*, 1993, **48**, 4978.
38 S. Grimme, J. Antony, S. Ehrlich and H. Krieg, *J. Chem. Phys.*, 2010, **132**, 154104.
39 H. J. Monkhorst and J. D. Pack, *Phys. Rev. B: Solid State*, 1976, **13**, 5188–5192.
40 S. Sayas, N. Morlanés, S. P. Katikaneni, A. Harale, B. Solami and J. Gascon, *Catal. Sci. Technol.*, 2020, **10**, 5027–5035.
41 L. Gurrala, M. M. Kumar, A. Yerrayya, P. Kandasamy, P. Castaño, T. Raja, G. Pilloni, C. Paek and R. Vinu, *Bioresour. Technol.*, 2022, **344**, 126204.
42 N. Morlanés, G. Lezcano, A. Yerrayya, J. Mazumder and P. Castaño, *Chem. Eng. J.*, 2022, **433**, 133201.
43 Z. Jiang, P. Qin and T. Fang, *Chem. Phys.*, 2014, **445**, 59–67.
44 W. Huang, W. Lai and D. Xie, *Surf. Sci.*, 2008, **602**, 1288–1294.
45 Y. Zhang, X. Xiao, Y. Cao, Y. Cai and J. Wang, *Int. J. Hydrogen Energy*, 2013, **38**, 2965–2972.
46 X. Gong, Y. Gu, N. Li, H. Zhao, C. Jia and Y. Du, *Inorg. Chem.*, 2016, **55**, 3992–3999.
47 J. A. Herron, S. Tonelli and M. Mavrikakis, *Surf. Sci.*, 2012, **606**, 1670–1679.
48 Z. Jiang, Q. Pan, M. Li, T. Yan and T. Fang, *Appl. Surf. Sci.*, 2014, **292**, 494–499.
49 C. He, H. Wang, L. Huai and J. Liu, *J. Phys. Chem. C*, 2012, **116**, 24035–24045.
50 S. C. Yeo, S. S. Han and H. M. Lee, *J. Phys. Chem. C*, 2014, **118**, 5309–5316.
51 F. F. Ma, S. H. Ma, Z. Y. Jiao and X. Q. Dai, *Appl. Surf. Sci.*, 2017, **405**, 71–78.
52 L. Huo, X. Han, L. Zhang, B. Liu, R. Gao and B. Cao, *Appl. Catal., B*, 2021, **294**, 120254.